Spatial-temporal dynamics at the interface of 3D printed photocurable thermoset resin layers

Benjamin M. Yavitt^{1,2}, Lutz Wiegart², Daniel Salatto¹, Zhixing Huang¹, Leonidas Tsapatsaris¹, Maya K. Endoh¹, Sascha Poeller³, Manuel Schiel³, Stanislas Petrash^{4,*}, Tadanori Koga^{1,5*}

¹Department of Materials Science and Chemical Engineering, Stony Brook University, Stony Brook, New York 11794-2275

²National Synchrotron Light Source II, Brookhaven National Laboratory, Upton, New York, 11973

³Adhesive Technologies, Henkel AG & Co KGaA, 40589 Duesseldorf, Germany

⁴Adhesive Technologies, Henkel Corporation, Bridgewater, New Jersey, 08807

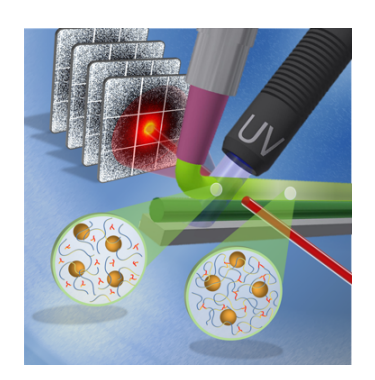
⁵Department of Chemistry, Stony Brook University, Stony Brook, New York 11794-3400

Abstract

Additive manufacturing (AM) is used to fabricate polymeric materials into complex threedimensional (3D) structures. As the 3D structure is built by sequential layer-by-layer deposition of filaments dispensed from a translating nozzle (in the case of extrusion-based printing), defects often form at the filament-filament interface. The out-of-equilibrium structural development that occurs during the printing process is difficult to directly measure by quantitative means, limiting our understanding of the physical mechanisms at play. Here, we utilize in-operando X-ray photon correlation spectroscopy (XPCS) measurements with microbeam capability to probe the real-time structural evolution at the filament-filament interface during extrusion 3D printing. We investigate the solidification of a dual cure (UV/thermal) acrylate/epoxy resin during multilayer 3D printing as a rational model by tracking the nanoscale motion of filler particles embedded in the resin. The spatially and temporally resolved dynamics (on length scales from several nm to a few hundreds of nm and timescales of $10^{-3} < t < 10^3$ seconds) are measured during the deposition of a single filament as well as during the deposition of a second layer on top of the cured underlayer. The addition of a second layer introduces structural perturbations at the interface and results in accelerated interfacial dynamics compared to those of the cured underlayer. However, as time proceeds, the local dynamical heterogeneity disappears, and the evolution of the dynamics progresses uniformly within the entire interfacial region. The homogeneity across the interface results from the formation of an interpenetrated epoxy network that spans across the first and second filaments. This homogenous interface is responsible for the isotropic tensile properties of a 3D printed sample that are independent of print direction and nearly the same as the bulk (non-3D printed) sample. The XPCS microrheology approach provides insight into the dynamicsprocess-property relationship at the printed filament interfaces.

Keywords: X-ray photon correlation spectroscopy, multilayer 3D printing, acrylate/epoxy, crosslinking, interfacial spatio-temporal dynamics

For Table of Content use only



Introduction

Additive manufacturing (AM), also known as "3D printing", is an attractive approach for building 3D objects and is utilized in several important industries. 1-5 Extrusion-based AM is one of the most popular and widespread techniques. Filaments are deposited onto a print bed by extrusion through a nozzle attached to a translating print head. 3D printed polymeric parts often suffer from limited adhesion at the filament-filament interface as the material requires time to diffuse between adjacent filaments, which may not be available during the rapid timescales of material solidification in conventional 3D printing.^{6,7} For polymers, a chain orientation induced during printing creates additional barriers toward successful entanglements at the filamentfilament interface and produces undesirable anisotropy in the bulk mechanical properties.⁸ Void formation, caused by the incomplete filling of a material, is also a severe issue as the reduction in a filament-filament contact surface area restricts entanglement formation and may negatively impact the mechanical strength of the 3D-printed composite. 9 While several studies have addressed improving interfacial adhesion by incorporation of additives or postprinting processes, information about the out-of-equilibrium material physics that occurs during the 3D printing process is desired to understand and overcome these defects in the final 3D printed part.^{8,10-12} Atomic force microscopy (AFM), thermal imaging, and X-ray scattering have all been utilized to characterize the interfacial structure in 3D printed polymeric systems after printing. ^{6,12–14} However, the in-situ structure at the filament-filament interface is difficult to resolve on the relevant length and time scales of the printing process.

Synchrotron X-ray techniques provide many promising approaches to observe such behavior.^{15–18} Small angle X-ray scattering (SAXS) and wide angle X-ray scattering (WAXS) measurements are able to determine structure across a wide regime of length scales (angstrom to

hundreds of nanometers), while coherent scattering techniques such as X-ray photon correlation spectroscopy (XPCS) provide additional information related to the material physics across time scales (sub-millisecond to 1000s of seconds) relevant to the AM process. 19-25 We recently demonstrated the in-operando XPCS measurements during direct ink write (DIW) 3D printing of industrial dual cure acrylate/epoxy thermoset resin under ultra-violet (UV) light.²³ The resin contained a small fraction of inorganic barium sulfate particles (average diameter $\approx 2 \mu m$). While the particles are a necessary component to facilitate UV penetration²³, they conveniently act as internal dynamic probes to resolve the development of crosslinking by sensing the surrounding internal structure. 26-29 It was found that the probe dynamics were not diffusive 30 but "hyper diffusive" for all printing conditions, a process which has been observed in many soft matter systems such as highly loaded colloidal gels, concentrated emulsions, and entangled polymer nanocomposites. ^{26,27,31,32} The structural dynamics in a single filament were measured as a function of both print speed and UV intensity, where higher UV dose resulted in a greater extent of internal crosslinking structure formation.²³ Curiously, spatial heterogeneities were identified at the topmost surface of the printed filament, regarded as the "interfacial zone" where UV induced crosslinking appeared to be more extensive than in the bulk.

Here, we aim at resolving the interfacial spatio-temporal dynamics during a multilayer 3D printing process of the same dual cure acrylate/epoxy thermoset resin under industrially relevant in-operando 3D printing conditions. This system was developed to overcome limited interfacial adhesion associated with void formation during 3D printing by maintaining molecular mobility within the secondary (thermally activated) prepolymer even after UV cure.³³ As shown in Figure S1 (Supporting Information (SI)), micro-voids commonly found in thermoplastic polymers printed by a fused filament fabrication (FFF) method are significantly reduced. Diffusion at the filament-

filament interface forms an interpenetrated epoxy network that spans across filaments, thereby increasing the interlayer adhesion. As a result, the 3D printed samples show isotropic tensile properties (Young's Modulus and strain at break) that are independent of print direction and nearly the same as the bulk (non-3D printed) sample (Table S1). Microbeam XPCS measurements with this validated, model material system focuses on the structure formation exclusively at the interface, providing elaboration on the reinforcement mechanism. In this study, the second layer is printed after an appropriate waiting time to ensure the sufficient mechanical property of the first layer and preserve the mobility of material necessary for interfacial adhesion. The present study provides new insight into the time evolution of the network dynamics at the filament-filament interface, highlighting the mechanism underlying the formation of a homogenous interface and the correlation between the microscopic structural/dynamical properties and relevant macroscopic properties. Demonstration of this technique may also display its applicability to investigate this well-known problem in the thermoplastic polymers printed by FFF that show significantly poor interlayer adhesion.

Experimental

The 1K Dual Cure (Acrylate/Epoxy) LOCTITE® VP 10997-085 Adhesive system was provided by Henkel Corporation. Details of the sample have been described elsewhere. Resins were transferred to 3 ml extrusion cartridge (Nordson 7012083) and used without further modification. The resin contains 15.6 wt.% inorganic barium sulfate particles and 1.2 wt.% of boron nitride platelets (average thickness ≈ 2 µm, average length ≈ 50 µm). The small X-ray beam size and coherence limitation reduce scattering contribution from large platelets. The "dual cure" consists of a "UV active" component and a "thermally active" component. During printing,

the UV active acrylate is initiated by 3 wt.% of Irgacure 754, partially crosslinking the material enough for continuous and consecutive printing of additional layers. The barium sulfate filler is non-UV absorbing, which improves the uniform UV curing of the filament.³³ After 3D printing, a second stage thermal cure is performed ex-situ at 120 °C to complete the crosslinking of the epoxy resin into a tough thermoset part that was used for the mechanical property experiments (Table S1).

In-operando XPCS measurements were performed on a customized 3D printing experimental setup at the Coherent Hard X-ray (CHX, 11-ID) beamline at the National Synchrotron Light Source II (NSLS-II) of Brookhaven National Laboratory (BNL) (Figure 1).¹⁵ Full experimental details are available in the SI (including Figure S2) and a previous report.²³ A partially coherent X-ray beam with size 10 μm × 10 μm (full-width half-maximum) and energy of 9.65 keV (i.e., an X-ray wavelength of $\lambda = 0.128$ nm) was used with an Eiger X 4M (Dectris) photon counting area detector (75 μ m \times 75 μ m pixel size) at a sample-to-detector distance of 10.08 m. The entire printer setup was mounted onto the sample stage of the CHX beamline and translated to align the filament in-line with the X-ray beam as it was printed onto the print bed (Figure S2). An on-axis video camera (OAV) was used to assist in the alignment of the X-ray beam. Filaments of 15 mm in length were printed at a print speed of $v_x = 1$ mm/s and extrusion pressure P = 10 psi (68 kPa) through a 20 GA straight tip metal nozzle (an inner diameter = 610 μm, Nordson PN 7018163) connected to a pressure-controlled dispenser (Ultimus V, Nordson EFD). For the first filament layer, the distance between the nozzle and the print bed was kept constant at 610 µm (i.e., the diameter of the nozzle) for reproducible printing of the desired filament geometry. Measurements were performed with the X-ray beam at multiple heights (h) above the print bed throughout the filament ranging from $h = 50 \mu m$ to $h = 500 \mu m$ (Figure S2). At $h > 500 \mu m$, the scattering intensity from the single filament was too low for meaningful measurements due to the decreased scattering volume. See Figure S3 for OAV images of filament during printing. Dynamics were investigated by XPCS at various relative UV intensities (maximum intensity ≈ 100 mW/cm²). Independent data sets were collected during printing and curing. The intersection of the beam and the sample was vertically translated by a distance of $\Delta h = 50 \,\mu m$ between each scattering experiment to spatially resolve dynamics across the height of the filament. To measure interfacial dynamics during the deposition of an additional layer, the print head was raised by 550 μm (slightly larger than the approximate filament height of 500 μm) and a second filament was printed on top

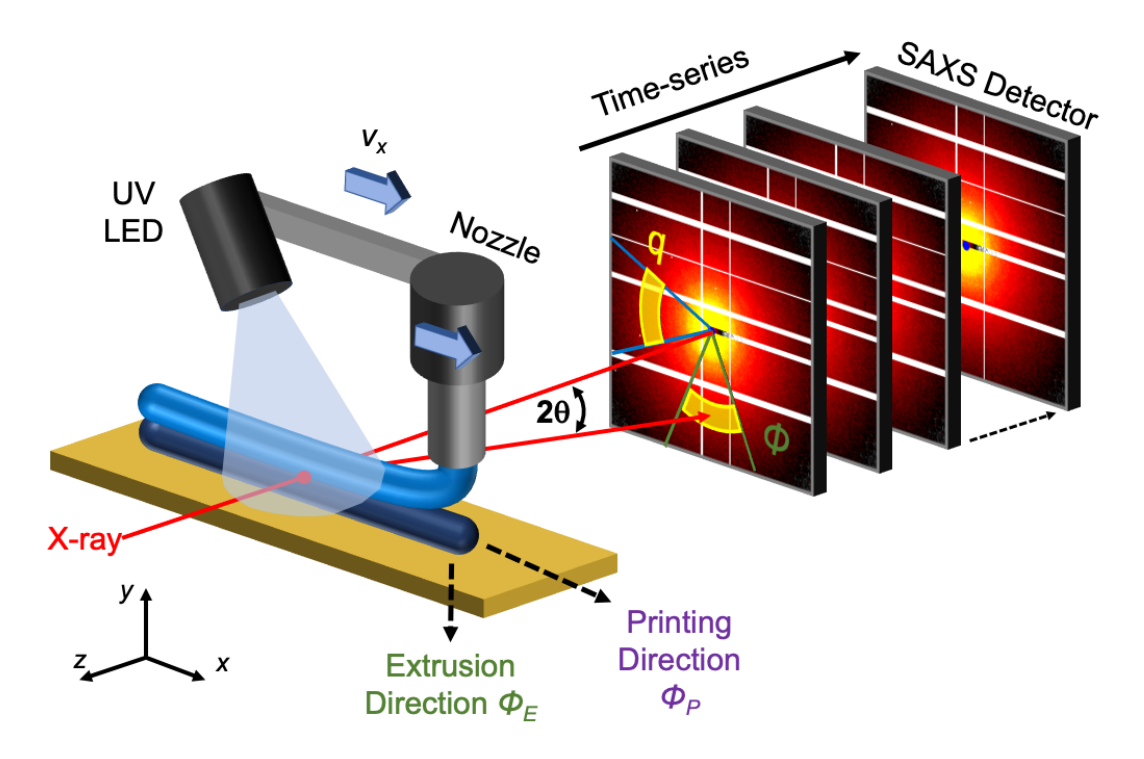


Figure 1. Experimental setup of double layer printing. Nozzle extrudes composite resin on top of UV-cured single layer after a constant wait time of $t_{wait} = 300$ s. A single 365 nm UV LED lamp (maximum intensity ~ 100 mW/cm²) was connected to the curing system and positioned with respect to the printhead with a stationary bracket. Deposition is in the x-direction at a velocity of magnitude v_x (in mm/s), perpendicular to incoming X-ray beam (along the z-direction). X-ray beam positioned on printed filament at height h with respect to the substrate (h = 0 μm) in the vicinity of the interface (h = 300 to h = 600 μm). Speckle patterns are collected on the 2D area SAXS detector placed behind the printing setup. Scattering pattern is masked into azimuthal slices of scattering vector q defined by scattering angle 2θ and angular slices of φ taken over a range of angles that cover the printing (φ_P) and extrusion (φ_E) directions. A time series of speckle patterns are collected to resolve out-of-equilibrium dynamics during 3D printing.

of the cured first filament after a constant wait time of $t_{wait} = 300$ s. The sample stage was positioned into the X-ray beam at several heights in the vicinity of the interface from h = 300 µm to h = 600 µm.

The analysis of the out-of-equilibrium scattering data and calculations of correlation functions were performed using CHX beamline Python code (NSLS-II GitHub).³⁸ Full analysis protocols are described in the previous report.²³ The dynamics are embodied in the time-resolved, ϕ -dependent autocorrelation function $g_2(q, \tau, \phi, t_{age}, h)$, where q is the scattering vector (0.02 nm⁻¹ $< q < 0.5 \text{ nm}^{-1}$, corresponding to length scales of ~10 to 300 nm), τ is the delay time, ϕ is the azimuthal angle on the 2D scattering pattern. The extrusion direction ϕ_E is vertical to the print bed and the printing direction ϕ_P is horizontal to the print bed. Due to the rapidly changing dynamics during the out-of-equilibrium printing process, $g_2(q, \tau, \phi, t_{age}, h)$ is obtained by averaging the two-time correlation function $C(q, \phi, t_1, t_2)$ over various average experimental aging times $t_{age} = (t_1 + t_2)/2$ where the dynamics are quasi-stationary:^{21,23}

$$C(q, \phi, t_1, t_2) = \frac{\langle I(q, t_1)I(q, t_2)\rangle}{\langle I(q, t_1)\rangle \langle I(q, t_2)\rangle} \tag{1}$$

where q is the magnitude of the scattering wavevector \mathbf{q} , $q = 4\pi\sin(\theta)/\lambda$ with 2θ being the scattering angle in the small angle scattering geometry[39.40].^{39,40} In practice, $C(q, \phi, t_1, t_2)$ is "cut" over a series of t_{age} with a lag time of $\tau = |t_2 - t_I|$, where each cut results in a g_2 which is fit to a Kohlrausch-Williams-Watts (KWW) form:

$$g_2 = c + \beta(\exp(-2(\Gamma \tau)^{\alpha})) \tag{2}$$

where β is the Siegert factor determined by the scattering setup and c is the baseline (expected to be 1 for ergodic samples). Quantities derived from XPCS experiments (such as α (q, t_{age} , h) and β (q, t_{age} , h)) are presented in Supporting Information (Figures S4-S7). We find $\beta \approx 0.18$ for the 3D

printing resin is comparable to a static sample (CoralPor®, Schott), suggesting that any faster dynamics outside of the experimental time window were not missed by the measurement. The baseline c is also found to be close to 1. Non-ergodicity may be expected for solid materials, indicating that the resin is not completely "solid-like" on the nanoscale and in the observable time regime. The relaxation rate Γ (in units of s⁻¹) and exponent α describe the timescale and shape of the relaxation process at each q, ϕ , t_{age} , and h. The dynamics are characterized by the linear ballistic motion model^{27,30,39,41}, i.e., $\Gamma = V_p q$ (Figure 2), where the proportionality constant V_p describes the q-independent dynamics. Due to the linear relationship, V_p represents the ballistic motion as a local displacement velocity (in the unit of nm/s) as opposed to $\Gamma \propto D_0 q^2$ identified for Brownian diffusion. We confirmed the linear scaling of Γ with q regardless of the choice of ϕ , t_{age} , and h. The dynamics in the observable q-regime are due to the constructive interference between filler and resin on length scales smaller than the filler themselves. Therefore, V_p is not strongly impacted

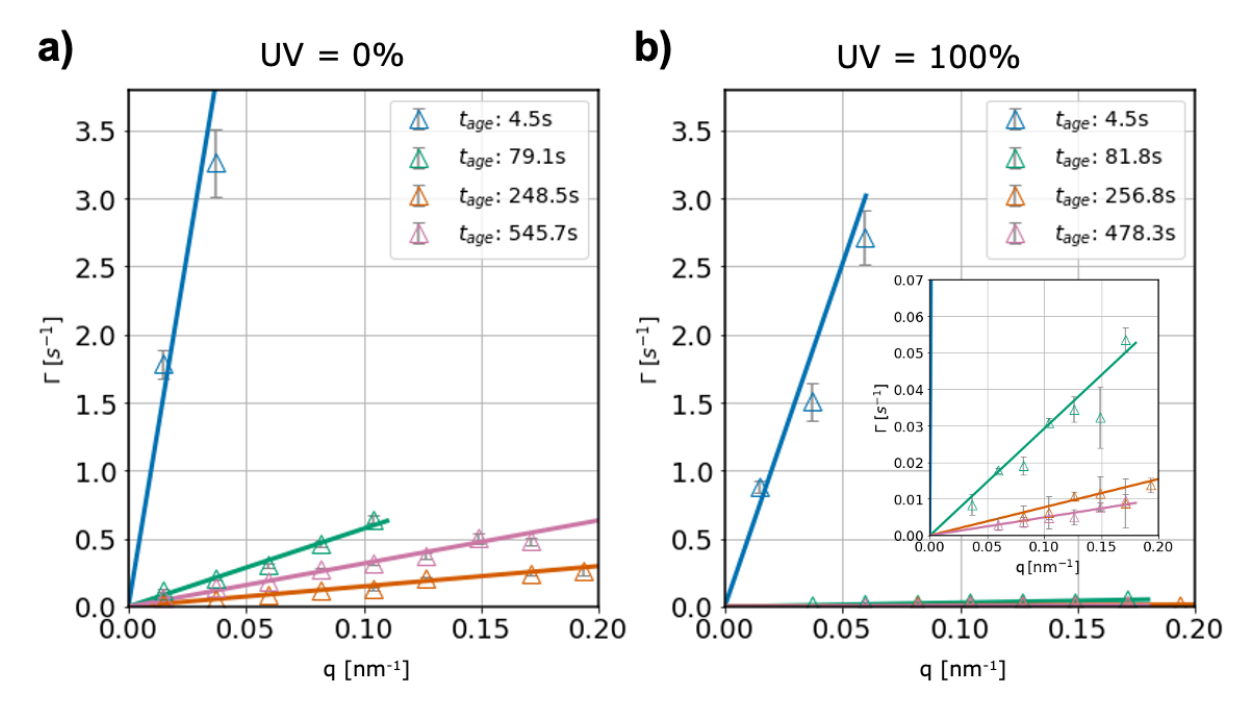


Figure 2. Relaxation rate (Γ) vs. q and corresponding fits to a linear, ballistic motion model where $\Gamma = V_p q$. V_p is the local displacement velocity of the fillers. Representative plots of a) 0% UV and b) 100% UV at $h = 300 \, \mu m$.

by the particle shape or size dispersity, which would be resolved at a much lower q regime. The length scales accessed by XPCS probe the dynamical behavior, critical to the polymer network structure formation (10 – 100 nm).

Results and Discussion

Single-layer printing. Before discussion of the spatial-temporal evolution at the interface, spatialtemporal evolution maps for the first filament layer were constructed from the compiled datasets of $V_p(\phi, t_{age}, h)$. Figure 3 shows the dynamics collected for the single filament in the extrusion direction (ϕ_E , vertical to the print bed) up to $t_{age} = 600$ s under 0%, 1%, 10%, and 100% UV intensity. The results parallel to the print bed (denoted as a ϕ_P) are summarized in Figure S8. The dynamics cover a wide range of timescales from $V_p \sim 10^2$ nm/s at 0% UV to 10⁻¹ nm/s at 100% UV, again highlighting the impact of the UV-triggered crosslinking, accompanying structure formation, and restriction of the filler motion. Here we present the structural dynamics resolved as a function of h, revealing the effect of UV absorption profile through the filament, as well as the competition of crosslinking with shear, elongational, and relaxation processes present during extrusion. Under 0% UV (Figure 3a), the progression of dynamics with t_{age} is rather uniform despite some heterogeneous pockets of V_p at h = 450 um for $t_{age} > 100$ s where the dynamics are faster compared to the locations in the filament at lower h. At $t_{age} = 500$ s, the dynamics at the upper interface is not resolvable (represented in white in Figure 3a) as the filament settles out of the X-ray beam. Dynamic information appears missing in this region because the scattering intensity decreases below the observable limit, identifying the macroscopic impact of the relaxation processes and limited shape retention in the absence of crosslinking.

Upon UV irradiation (Figures 3b-d), the overall dynamics become slower with increasing the UV intensity. Heterogeneous behavior of V_p in both t_{age} and h is observed at all UV conditions with "bands" progressing across various values of h. Especially, at 100 % UV intensity, as time progresses, the interfacial zone at the top surface of the filament (at $h > 450 \mu m$) emerges, indicating a higher degree of crosslinking compared to the center of the filament at the respective t_{age} . The slow dynamics layer in the interfacial zone clearly forms at $t_{age} \approx 300 \text{ s}$ (i.e., the black region in Figure 3d, representing at $V_p < 0.01 \text{ nm/s}$ for dynamics slower than the observable time window set by the XPCS measurements). The filament is bisected as the dynamic timescale below $h = 300 \mu m$ is clearly faster compared to dynamics in the vicinity of the interfacial zone at $h > 450 \mu m$ (Figure 3d). It should be noted that based on the scattering setup, the observed dynamics are "averaged" along the beam direction which traverses through bulk regions of the filament as well

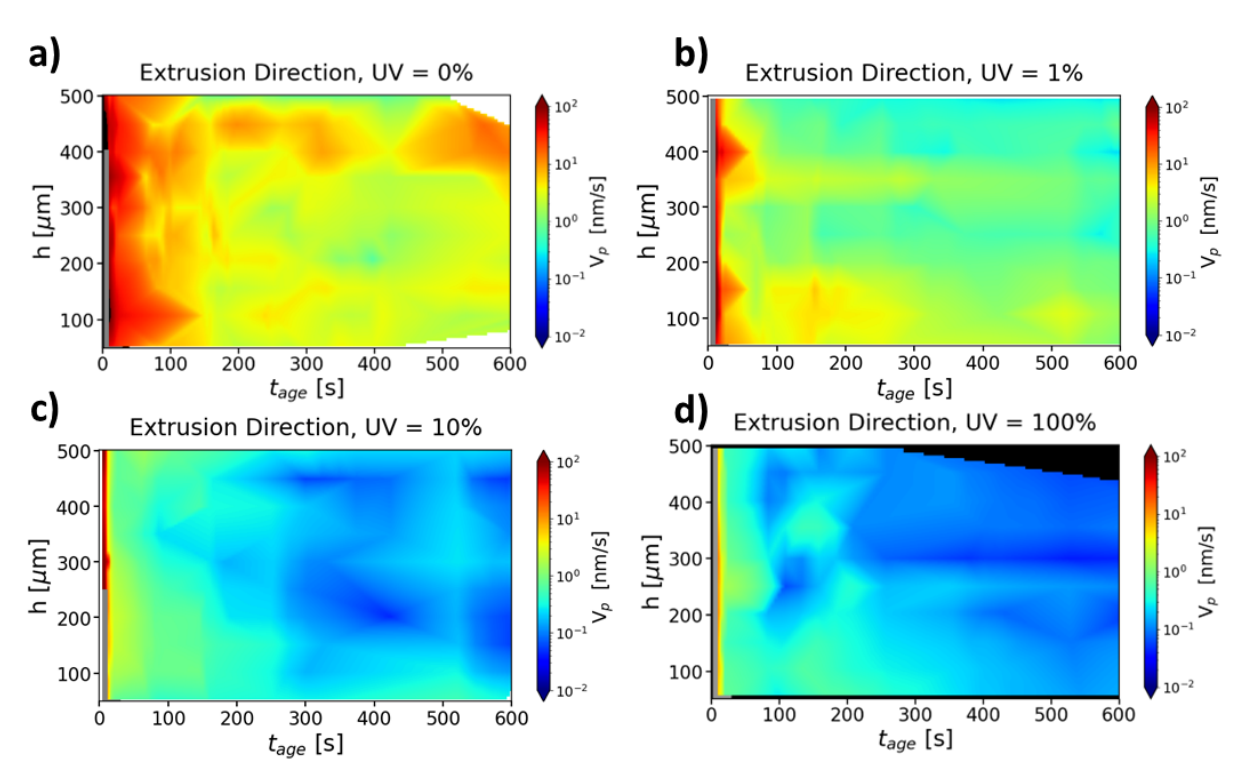


Figure 3. Spatial-temporal evolution of the nanoscale dynamics represented by the ballistic mobility of inorganic filler particles $V_p(h, t_{age})$ shown for in-situ prints across a range of UV intensities: (a) 0% UV, (b) 1% intensity, (c) 10% intensity, and (d) 100% UV intensity. Dynamics are shown in the vertical extrusion direction (ϕ_E) .

as the material exposed at the top surface of the interfacial zone. Assuming the structure formation in these regions is different due to penetration of the UV and progression of crosslinking, contributions from each region along the cross section may produce complicated correlation functions that may not be described by the KWW form. However, as will be discussed in Figure 6, we confirmed that all g_2 functions could be fit with a single KWW function. Hence, the scattering signal is mostly dominated by the bulk regions especially at low h, assuming the immediate surface layer of the filament is thin, and UV hits the top surface more than the side of the filament.

The early t_{age} is of interest as the initial shape retention of the filament under direct UV illumination (3 s < t_{age} < 15 s) is resolved. In Figure 4, the dynamics are shown for ϕ_E (extrusion

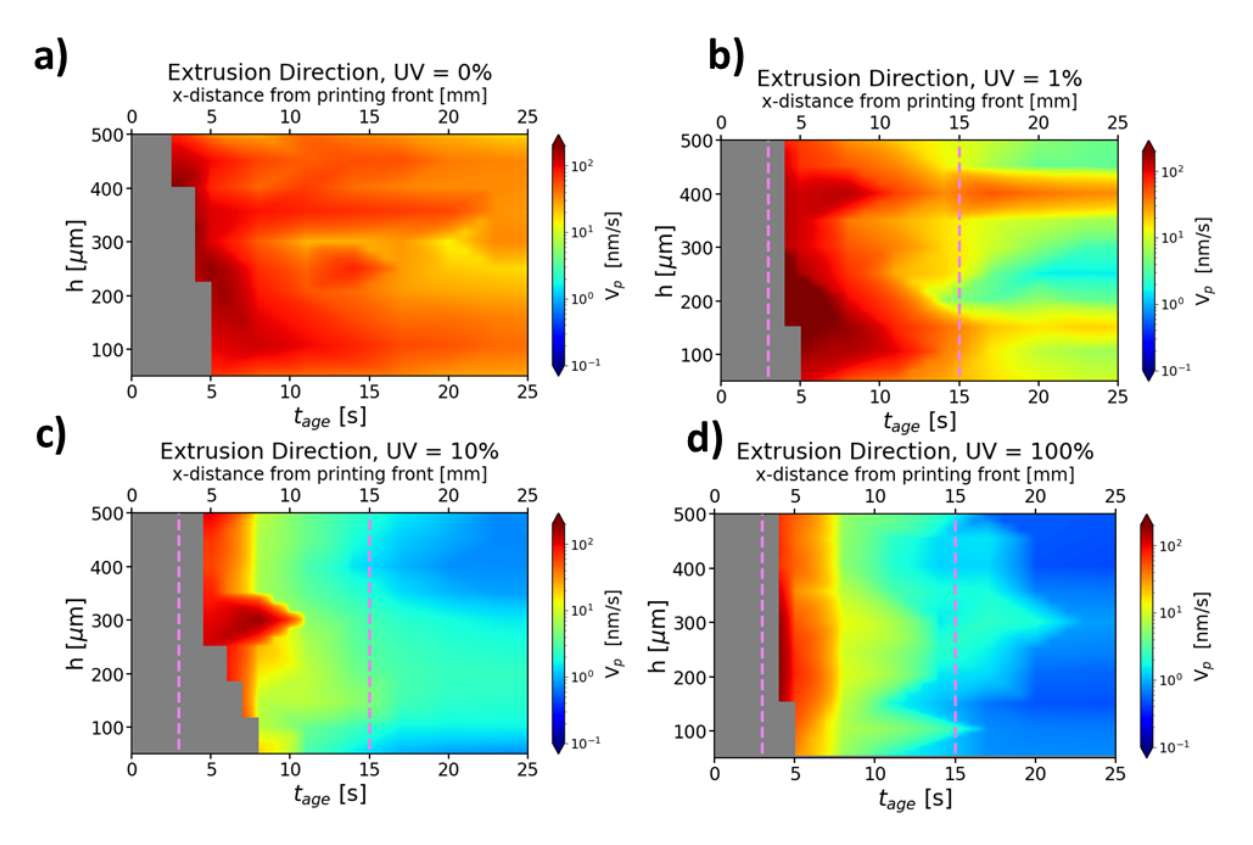


Figure 4. Expanded spatial-temporal evolution of the nanoscale dynamics shown in Figure 3 within the timescales up to $t_{age} = 25$ s: (a) 0% UV, (b) 1% intensity, (c) 10% intensity, and (d) 100% UV intensity. Time interval of direct UV illumination ($t_{UV} = 12s$) is indicated by the dashed vertical lines. Note that the color scale bars to represent V_p are different from that used for Figure 3.

direction) at the earliest times. The dynamics generally form an asymmetric front of relaxation processes (see also Figure S8 for the dynamics in ϕ_P (printing direction)). In all cases at $t_{age} < 3$ s, the dynamics are too fast to be resolved (above the fastest observable limit of $V_P \approx 100$ nm/s), limited by the scattering signal and dose limit (to avoid X-ray beam damage of the sample). Therefore, these missing values of V_P are represented in grey. The UV illumination is shown in Figure 4 accompanied by the timeframe of t_{UV} marked by the dashed vertical lines (the total UV exposure time, $t_{UV} = 12$ s). The dynamics in this direction still reach a uniform state as a function of h at $t_{age} = 25$ s regardless of the choice of UV intensity.

Double-layer printing. After demonstrating the sensitivity of microbeam measurements on the single filament, multilayer printing was investigated using the spatial-temporal approach. Before in-operando XPCS experiments, we confirmed that the resins under 1% and 10% UV illumination with $t_{UV} = 12s$ collapsed onto each other during double-layer printing and did not hold the shape, rendering the identification of the interface difficult. This also emphasizes the importance of using a sufficient UV dose to successfully print multilayers. For this reason, we conducted the XPCS experiments only at 100% UV intensity with $t_{UV} = 12s$. In Figure 5, $t_{age} = 0$ s references the time at which the second layer crosses the X-ray beam during printing at a wait time $t_{wait} = 300$ s after deposition of the first layer, which is observed in real-time by the on-axis microscope camera. Therefore, the global aging time with respect to the printing of the first layer is effectively shifted by t_{wait} (shown on the alternate x-axis of $t_{age} + t_{wait}$ in Figure 5a).

The area of interest is around the interface of the two filaments (i.e., $300 \, \mu m < h < 600 \, \mu m$) as the dynamics are expected to be influenced by the deposition of the second layer. The approximate location of the filament-filament interface ($h \approx 500 \, \mu m$) is indicated by the white

dotted line in Figure 5a. As shown in Figure 3d, for $300 < h < 500 \mu m$ in the single filament at 100% UV, V_p slows down to $\sim 10^{-1}$ nm/s after several hundreds of seconds. In contrast, during the deposition of a new filament, the dynamics of the first (bottom) filament speed up by an order of

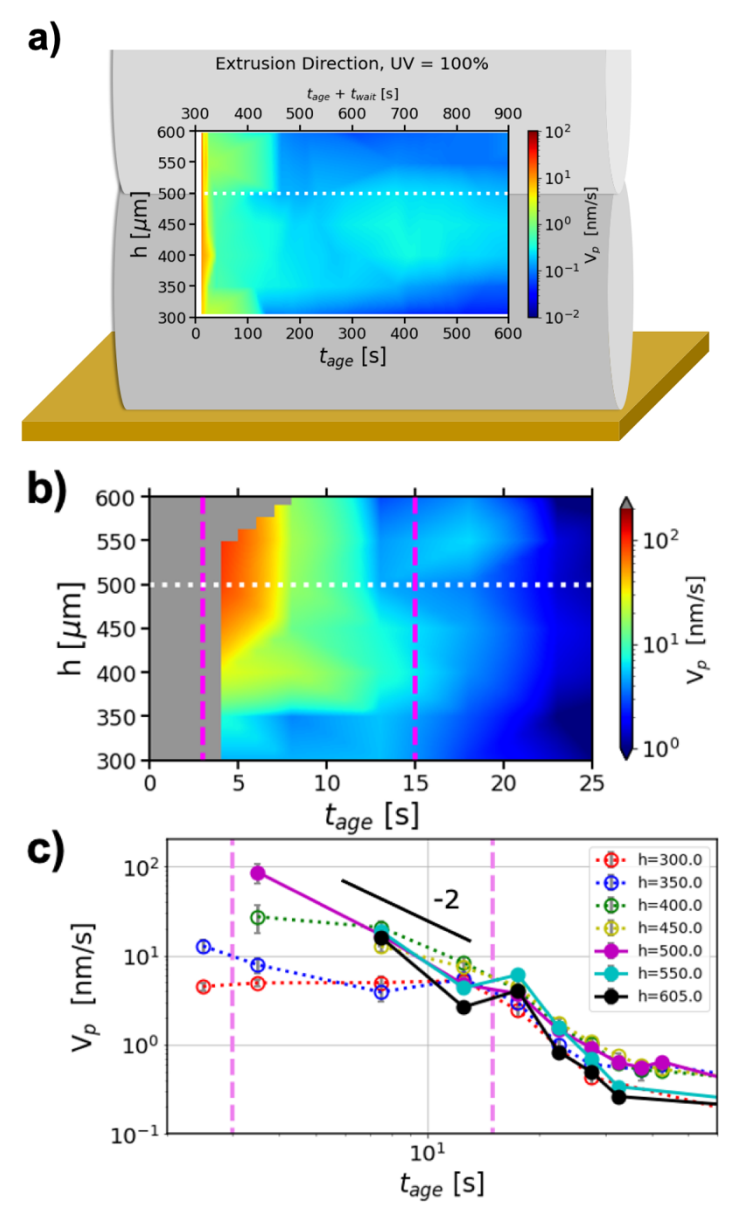


Figure 5. Dynamic evolution of multilayer printing under 100% UV where h [µm] is the height with respect to the print bed h=0. Dynamics are presented in the vertical extrusion direction (φ_E). Approximate location of the filament-filament interface is indicated by the white dotted line. a) Evolution of V_p during multilayer printing at t_{age} corresponding to the active deposition of the top filament. b) In-situ timescales up to $t_{age}=25$ s. c) Plots of V_p vs. t_{age} for each height illustrating the power law relationship $m=d(\log(V_p))/d(\log(t_{age}))$, especially in the time interval of UV illumination from $t_{age}=3$ s to 15 s indicated by the dashed vertical lines. Power law decay is non-uniform as m becomes steeper in the vicinity of the interface. After UV illumination, the evolution of the dynamics becomes height independent.

magnitude (up to $V_p \sim 10^0$ nm/s) which persist for several hundreds of seconds as the top layer cures and relaxes (Figure 5a). Several factors contribute to the rejuvenation of these dynamics. At the interfacial zone of $h = 450 \mu m$, the introduction of new resin from the second layer overlaps the first layer to ensure strong interlayer adhesion (Figure S3c). The measured dynamics are "averaged" along the beam direction and include contributions from material in the "cured" bottom and the "fresh" top layer, where the relative contribution is based on the curvature of the filament. The perturbation by the stress exerted from the weight of the new material induces additional dynamics near and below the filament-filament interface (h = 300 to 400 µm) which presumably rebounds with some elasticity.²² The fact that the dynamics are faster in the first filament as compared to the "cured" single filament (shown in Figure 3d) confirms that the internal structure of the first filament is only partially cured, according to the resin design. As a result, the first filament still allows the diffusion of uncured epoxy at the interface, facilitating the formation of an interpenetrated network that spans the filaments and increases the interlayer adhesion. As will be discussed below, the homogenous interface is developed quickly after $t_{age} = 15$ s (Figure 5b). In addition, as shown in Figure S9a, similar accelerated dynamics of the first filament at 300 μ m < h< 500 µm compared to the bottom filament (shown in Figure S8d) are observed in the print direction (ϕ_P). In this study, the second layer was printed at a waiting time of t_{wait} = 300 s to develop a sufficient mechanical property during double-layer printing and preserve the mobility of material necessary for interfacial adhesion. Future investigations are required to reveal heterogeneities and interfacial boundaries in case of printing a second layer on top of a filament that is cured to a higher degree, for example, after a waiting time of $t_{wait} = 600 \text{ s.}$

The interfacial structure development at the early t_{age} is also highlighted in Figure 5b. It should be noted that the color scale bars to represent the range of V_p are different from those used

for Figure 5a. Upon deposition and UV curing, it was found that the progression of V_p is surprisingly uniform in the vicinity of the filament-filament interface, i.e., $h = 500 \, \mu m$. The data also indicates the local dynamical heterogeneity at $t_{age} < 13 \, s$: the interfacial dynamics are much faster than the cured underlayer located at around $h = 300 \, \mu m$. Similar behavior is identified in the ϕ_P direction (Figure S9b). These results again highlight the effect of the stress exerted from the weight of new material, inducing additional dynamics near the filament-filament interface. However, the local dynamical heterogeneity disappeared as time proceeded, and the homogenous interface is then developed.

To further provide insight into the interfacial dynamics at the early t_{age} , the height dependence of these transient dynamics in the vertical extrusion direction (φ_E) is summarized in Figure 5c. During UV illumination, the dynamics within the bottom filament at $h \leq 350 \, \mu m$ are rather static. On the other hand, at $h > 350 \, \mu m$, V_p decays with a power-law exponent (m) of about -2 (i.e., $V_p \sim t_{age}^{-2}$), close to the power law exponent of -3 reported for single filament sample under the same UV dose.²³ After $t_{age} = 13$ s, the evolution of the dynamics progresses uniformly within the entire interfacial region and collapses into a single front in terms of both V_p and m. The homogeneity across the interface results from the formation of an interpenetrated epoxy network that spans across the first and second filaments.

Additional microscopic details of the multilayer printing experiments are interrogated through the lens of time-resolved autocorrelation functions g_2 . Figures 6a-6c show typical g_2 at various t_{age} and representative q = 0.037 nm⁻¹ in the extrusion direction (φ_E) under 100% UV intensity. g_2 is normalized by c and β (eq. 2). Three representative heights in the vicinity of the filament-filament interface are shown. The corresponding KWW fits are shown by the solid lines. Overall, g_2 follows an expected exponential decay with increasing delay time τ where the

characteristic time scale of the relaxation event increases with increasing t_{age} , indicating the

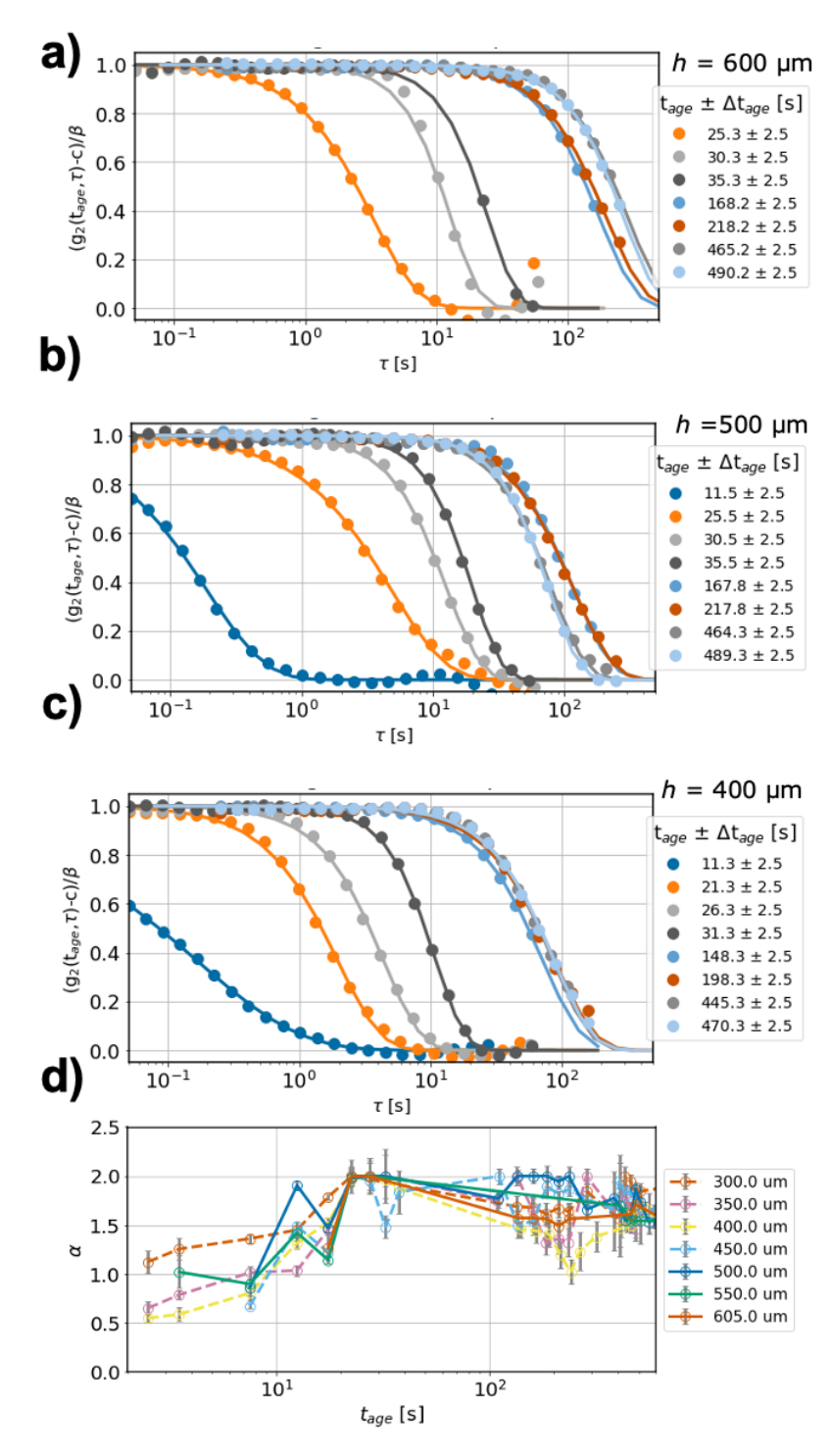


Figure 6. Normalized one-time correlation functions g_2 for representative t_{age} measured at different heights in filaments cured under 100% UV intensity: a) $h = 600 \mu m$, b) 500 μm and c) 400 μm. Dynamics are presented in the vertical extrusion direction $φ_E$. Symbols represent the calculated g_2 functions while lines show fits to a KWW stretched/compressed exponential function. d) Trend in the stretching exponent as a function of h and t_{age} in the vertical extrusion direction $φ_E$.

internal dynamics of the filler particles slow down as the second filament is printed and cured.

The shape of g_2 is also of interest, embodied in the stretching/compression exponent α which represents the emergence of multiple relaxation processes in the disordered system.⁴² In Figure 6d, the values of h corresponding to the locations within the first filament ($h \le 450 \mu m$) are represented by a dashed line, while the locations at the interface and within the second layer ($h \ge 500 \mu m$) are represented by a solid line. From the figure, we can see that at an early t_{age} ($t_{age} < 10 \text{ s}$), α is close to 1 but quickly begins to approach $\alpha = 1.5$ or higher, indicating that the relaxation becomes compressed (i.e., faster than an exponential decay). Coupled the exponent of 1.5 with the linear relationship of Γ and q (as demonstrated in Figure 2), the dynamics follow a hyper-diffusive motif.³⁰ In contrast, in the absence of UV, α does not show as sharp of an increase in the early stages of t_{age} , beginning around $\alpha \sim 1$ and then gradually fluctuating around $\alpha \sim 1.5$ with increasing t_{age} (Figure S4). Thus, the abrupt change in α at the interface region is indicative of the formation of a network structure.

Moreover, the general scaling of $\Gamma \propto q^1$ along with $\alpha = 1.5$ has been previously attributed to strain release of randomly distributed stress dipoles in hydrogels and aerogels. ^{39,43,44} More generally, Cipelletti and co-workers ³⁰ proposed that the deformation under the action of internal stresses is responsible for the final decay of the dynamic structure factor of a system (that is related to g_2), and α can be used as a qualitative measure of the internal stress for a wide variety of jammed soft materials. As Narayanan and co-workers ⁴² pointed out, stress fields may locally develop at the filler-resin interface due to poor wetting. The interaction of the fillers (whose surfaces were not modified) with the resin is favorable enough to adequately disperse the particles in the cured resin. However, as shown in Figure S1, there is the formation of some micron-size voids at the filler-resin interface due to the imperfect mixing of fillers and resin. The voids would allow the local

internal stress fields to dissipate quickly⁴⁵, resulting in a compressed exponential relaxation. In Figure 6d, α is close to 1 at $t_{age} < 10$ s, i.e., the least stressed state, suggesting the absence of an epoxy network formation. The network structure triggers the onset of a hyper-diffusive motion of the markers throughout the printed filament at $t_{age} > 15$ s. The compression of the relaxation decay after UV exposure $t_{age} > 15$ s within the entire interfacial region suggests that the crosslinked mesh of the polymer becomes arrested. However, as t_{age} further progresses, the gradual decrease in α (after $t_{age} \sim 30$ s), then a fluctuation of α reveals some stress release in the network (Figure 6d). These experimental results imply that the UV cure completes the interfacial crosslinking partially. In fact, the interfacial dynamics are still of the order of $V_p = 1$ nm/s at $t_{age} = 600$ s (Figure 5a), which is nearly two orders of magnitude higher than those of the cured single filament (Figure 3d). A second stage thermal cure at high temperatures (typically at 120 °C) after the UV cure completes the crosslinking of the filament-filament interface entirely, creating a tough 3D printed thermoset multilayer.

Conclusion

It is vital to create a uniform interface between adjacent filaments during 3D printing to improve interfacial adhesion and structural integrity. By using in-situ XPCS measurements, we have revealed the out-of-equilibrium structural development at the interface during the solidification of a dual cure (UV/thermal) thermoset resin upon multilayer 3D printing with in-situ UV curing. Measurements were performed with the X-ray microbeam at multiple heights (h) above the print bed throughout the filament. The approximate height of a single filament was 500 μ m. The dual cure system has been developed to overcome limited interfacial adhesion and reduce void formation during 3D printing. In this study, the second layer was printed at a waiting time (t_{wait} ,

the time between the printing of each layer) of 300 s, not only resulting in the sufficient mechanical property but also preserving the mobility of material necessary for interfacial adhesion during double-layer printing. The XPCS results elucidated that printing a second layer perturbs the semi-static structure of the first layer at the microscopic scale and results in the accelerated dynamics at the interface compared to those of the cured underlayer at around $h = 300 \, \mu m$. However, as time proceeded, the local dynamical heterogeneity disappeared, and the evolution of the dynamics progressed uniformly within the entire interfacial region. It is reasonable to conclude that the resultant homogenous interface contributes to the isotropic tensile properties that are independent of print direction and nearly the same as the bulk (non-3D printed) sample (Table S1). Furthermore, we found that the observed dynamics track the internal stress at the filler-resin interface during a crosslinking process.

The printing schedule (modulated through t_{wait}) is important to consider as the filament constantly evolves during the printing operation. If the second filament is deposited much later ($t_{wait} > 600 \text{ s}$), the highly crosslinked interfacial zone of the first filament (as shown in Figure 3d) is likely to hinder diffusion of additional resin across the filament-filament interface. On the other hand, if the second layer is deposited too early, the first layer may be perturbed more drastically and take longer to recover or not possess the necessary shape retention to support a second layer at all. The necessary wait time for a steady state is on the order of $t_{wait} \sim 100 \text{ s}$ according to this investigation, which is rather significant for many rapid industrial printing applications. Traditionally, the process optimization would be investigated indirectly by printing a set of parts followed by ex-situ structural characterization and correlation. Here, in-situ XPCS produces real time visualization of the structural dynamics and unravels transient inhomogeneities that dictate the performance and integrity of the 3D printed piece. The novelty and design of the dual cure

thermoset resin is shown to facilitate formation of a uniform interface between two filaments. Future investigations into thermoplastic polymers printed via FFF could reveal crucial information as well for understanding the adhesion mechanisms and improve part performance and integrity.

SUPPORTING INFORMATION. The Supporting Information is available free of charge online:

Table S1. Mechanical properties of dual cure acrylate/epoxy thermoset resin (1K LOCTITE® VP 10997-085) adhesive system.

Figure S1. X-ray tomography measurements for the Dual Cure Resin used for the present study).

Figure S2. Photograph of in-situ DIW 3D printing/XPCS experimental set up.

Figure S3. On axis video microscope images of the filament during printing.

Figure S4. Quantities derived from KWW fitting of XPCS datasets for 0% UV intensity.

Figure S5. Quantities derived from KWW fitting of XPCS datasets for 1% UV intensity.

Figure S6. Quantities derived from KWW fitting of XPCS datasets for 10% UV intensity.

Figure S7. Quantities derived from KWW fitting of XPCS datasets for 100% UV intensity.

Figure S8. Spatial-temporal evolution of nanoscale dynamics represented by the ballistic

mobility of inorganic filler particles shown for in-situ prints across a range of UV

intensities in the horizontal printing direction.

Figure S9. Dynamic evolution of multilayer printing under 100% UV intensity.

Corresponding Authors

*E-mail: tadanori.koga@stonybrook.edu (T.K.)

*E-mail: stan.petrash@henkel.com (S.P.)

Notes

Portions of the materials described in this manuscript is patent pending. LOCTITE® is a registered

trademark of Henkel and its affiliates in the US and elsewhere. All other marks are trademarks of

their respective owners.

Acknowledgements

B.M.Y. and T.K. acknowledge financial support from Henkel Corporation and Brookhaven

National Laboratory. Acknowledgment is also made to the Donors of the American Chemical

Society Petroleum Research Fund (ACS-PRF 59064-ND7) for partial support of this research.

T.K. also acknowledges partial financial supports from National Science Foundation (DMR

2210207 and DGE 1922639). This work used resources of the National Synchrotron Light Source

II (Beamline 11-ID), which is a U.S. DOE Office of Science Facility, at Brookhaven National

Laboratory under Contract No. DE-SC0012704. The authors thank Andrei Fluerasu, Yugang

Zhang, Ronald Pindak, and Maria Torres Arango at NSLS-II for their help developing the

experiments and discussing the results.

References

Ngo, T. D.; Kashani, A.; Imbalzano, G.; Nguyen, K. T. Q.; Hui, D. Additive Manufacturing (1)

(3D Printing): A Review of Materials, Methods, Applications and Challenges. Compos.

23

- Part B Eng. 2018, 143, 172–196.
- (2) Truby, R. L.; Lewis, J. A. Printing Soft Matter in Three Dimensions. *Nature* **2016**, *540* (7633), 371–378.
- (3) Li, L.; Lin, Q.; Tang, M.; Duncan, A. J. E.; Ke, C. Advanced Polymer Designs for Direct-Ink-Write 3D Printing. *Chem. A Eur. J.* **2019**, *25* (46), 10768–10781.
- (4) Boydston, A. J.; Cao, B.; Nelson, A.; Ono, R. J.; Saha, A.; Schwartz, J. J.; Thrasher, C. J. Additive Manufacturing with Stimuli-Responsive Materials. *J. Mater. Chem. A* **2018**, *6* (42), 20621–20645.
- (5) Narupai, B.; Nelson, A. 100th Anniversary of Macromolecular Science Viewpoint: Macromolecular Materials for Additive Manufacturing. *ACS Macro Lett.* **2020**, *9* (5), 627–638.
- (6) Seppala, J. E.; Han, S. H.; Hillgartner, K. E.; Davis, C. S.; Migler, K. B. Weld Formation during Material Extrusion Additive Manufacturing. *Soft Matter* **2017**, *13* (38), 6761–6769.
- (7) Davis, C. S.; Hillgartner, K. E.; Han, S. H.; Seppala, J. E. Mechanical Strength of Welding Zones Produced by Polymer Extrusion Additive Manufacturing. *Addit. Manuf.* **2017**, *16*, 162–166.
- (8) Levenhagen, N. P.; Dadmun, M. D. Improving Interlayer Adhesion in 3D Printing with Surface Segregating Additives: Improving the Isotropy of Acrylonitrile-Butadiene-Styrene Parts. *ACS Appl. Polym. Mater.* **2019**, *1* (4), 876–884.
- (9) Xu, W.; Jambhulkar, S.; Zhu, Y.; Ravichandran, D.; Kakarla, M.; Vernon, B.; Lott, D. G.; Cornella, J. L.; Shefi, O.; Miquelard-Garnier, G.; Yang, Y.; Song, K. 3D Printing for Polymer/Particle-Based Processing: A Review. *Compos. Part B Eng.* 2021, 223 (June), 109102.

- (10) Street, D. P.; Mah, A. H.; Patterson, S.; Pickel, D. L.; Bergman, J. A.; Stein, G. E.; Messman, J. M.; Kilbey, S. M. Interfacial Interactions in PMMA/Silica Nanocomposites Enhance the Performance of Parts Created by Fused Filament Fabrication. *Polymer* 2018, 157, 87–94.
- (11) Street, D. P.; Ledford, W. K.; Allison, A. A.; Patterson, S.; Pickel, D. L.; Lokitz, B. S.; Messman, J. M.; Michael Kilbey, S. Self-Complementary Multiple Hydrogen-Bonding Additives Enhance Thermomechanical Properties of 3D-Printed PMMA Structures. *Macromolecules* 2019, 52 (15), 5574–5582.
- Gojzewski, H.; Guo, Z.; Grzelachowska, W.; Ridwan, M. G.; Hempenius, M. A.; Grijpma,
 D. W.; Vancso, G. J. Layer-by-Layer Printing of Photopolymers in 3D: How Weak Is the
 Interface? ACS Appl. Mater. Interfaces 2020, 12 (7), 8908–8914.
- (13) Trigg, E. B.; Hmeidat, N. S.; Smieska, L. M.; Woll, A. R.; Compton, B. G.; Koerner, H. Revealing Filler Morphology in 3D-Printed Thermoset Nanocomposites by Scanning Microbeam X-Ray Scattering. *Addit. Manuf.* **2021**, *37*, 101729.
- (14) Abbott, A. C.; Tandon, G. P.; Bradford, R. L.; Koerner, H.; Baur, J. W. Process-Structure-Property Effects on ABS Bond Strength in Fused Filament Fabrication. *Addit. Manuf.* **2018**, *19*, 29–38.
- Wiegart, L.; Doerk, G. S.; Fukuto, M.; Lee, S.; Li, R.; Marom, G.; Noack, M. M.; Osuji, C.
 O.; Rafailovich, M. H.; Sethian, J. A.; Shmueli, Y.; Torres Arango, M.; Toth, K.; Yager, K.
 G.; Pindak, R. Instrumentation for In Situ/Operando X-Ray Scattering Studies of Polymer Additive Manufacturing Processes. *Synchrotron Radiat. News* 2019, *32* (2), 20–27.
- (16) Shmueli, Y.; Lin, Y. C.; Lee, S.; Zhernenkov, M.; Tannenbaum, R.; Marom, G.; Rafailovich, M. H. In Situ Time-Resolved X-Ray Scattering Study of Isotactic

- Polypropylene in Additive Manufacturing. *ACS Appl. Mater. Interfaces* **2019**, *11* (40), 37112–37120.
- (17) Nogales, A.; Gutiérrez-Fernández, E.; García-Gutiérrez, M.-C.; Ezquerra, T. A.; Rebollar, E.; Šics, I.; Malfois, M.; Gaidukovs, S.; Gēcis, E.; Celms, K.; Bakradze, G. Structure Development in Polymers during Fused Filament Fabrication (FFF): An in Situ Small- And Wide-Angle X-Ray Scattering Study Using Synchrotron Radiation. *Macromolecules* 2019, 52 (24), 9715–9723.
- (18) Shmueli, Y.; Jiang, J.; Zhou, Y.; Xue, Y.; Chang, C. C.; Yuan, G.; Satija, S. K.; Lee, S.; Nam, C. Y.; Kim, T.; Marom, G.; Gersappe, D.; Rafailovich, M. H. Simultaneous in Situ X-Ray Scattering and Infrared Imaging of Polymer Extrusion in Additive Manufacturing. *ACS Appl. Polym. Mater.* **2019**, *1* (6), 1559–1567.
- (19) Leheny, R. L.; Rogers, M. C.; Chen, K.; Narayanan, S.; Harden, J. L. Rheo-XPCS. *Curr. Opin. Colloid Interface Sci.* **2015**, *20* (4), 261–271.
- (20) Nogales, A.; Fluerasu, A. X Ray Photon Correlation Spectroscopy for the Study of Polymer Dynamics. *Eur. Polym. J.* **2016**, *81*, 494–504.
- (21) Johnson, K. J.; Wiegart, L.; Abbott, A. C.; Johnson, E. B.; Baur, J. W.; Koerner, H. In Operando Monitoring of Dynamic Recovery in 3D-Printed Thermoset Nanocomposites by XPCS. *Langmuir* **2019**, *35* (26), 8758–8768.
- (22) Torres Arango, M. A.; Zhang, Y.; Li, R.; Doerk, G.; Fluerasu, A.; Wiegart, L. In-Operando Study of Shape Retention and Microstructure Development in a Hydrolyzing Sol-Gel Ink during 3D-Printing. *ACS Appl. Mater. Interfaces* **2020**, *12* (45), 51044–51056.
- (23) Yavitt, B. M.; Wiegart, L.; Salatto, D.; Huang, Z.; Endoh, M. K.; Poeller, S.; Petrash, S.; Koga, T. Structural Dynamics in UV Curable Resins Resolved by in Situ 3D Printing X-

- Ray Photon Correlation Spectroscopy. ACS Appl. Polym. Mater. 2020, 2 (9), 4096–4108.
- (24) Lin, C. H.; Dyro, K.; Chen, O.; Yen, D.; Zheng, B.; Arango, M. T.; Bhatia, S.; Sun, K.; Meng, Q.; Wiegart, L.; Chen-Wiegart, Y. C. K. Revealing Meso-Structure Dynamics in Additive Manufacturing of Energy Storage via Operando Coherent X-Ray Scattering. *Appl. Mater. Today* 2021, 24, 101075.
- (25) Torres Arango, M.; Zhang, Y.; Zhao, C.; Li, R.; Doerk, G.; Nykypanchuk, D.; Chen-Wiegart, Y. C. K.; Fluerasu, A.; Wiegart, L. Ink-Substrate Interactions during 3D Printing Revealed by Time-Resolved Coherent X-Ray Scattering. *Mater. Today Phys.* 2020, 14, 100220.
- (26) Guo, H.; Bourret, G.; Corbierre, M. K.; Rucareanu, S.; Lennox, R. B.; Laaziri, K.; Piche, L.; Sutton, M.; Harden, J. L.; Leheny, R. L. Nanoparticle Motion within Glassy Polymer Melts. *Phys. Rev. Lett.* 2009, 102 (7), 20–23.
- (27) Mangal, R.; Srivastava, S.; Narayanan, S.; Archer, L. A. Size-Dependent Particle Dynamics in Entangled Polymer Nanocomposites. *Langmuir* **2016**, *32* (2), 596–603.
- (28) Trigg, E. B.; Wiegart, L.; Fluerasu, A.; Koerner, H. Dynamics of Polymerization and Gelation in Epoxy Nanocomposites via X-Ray Photon Correlation Spectroscopy. *Macromolecules* **2021**, *54* (13), 6575–6584.
- (29) Yavitt, B. M.; Salatto, D.; Huang, Z.; Koga, Y. T.; Endoh, M. K.; Wiegart, L.; Poeller, S.; Petrash, S.; Koga, T. Revealing Nanoscale Dynamics during an Epoxy Curing Reaction with X-Ray Photon Correlation Spectroscopy. *J. Appl. Phys.* **2020**, *127*, 114701.
- (30) Cipelletti, L.; Ramos, L.; Manley, S.; Pitard, E.; Weitz, D. A.; Pashkovski, E. E.; Johansson,
 M. Universal Non-Diffusive Slow Dynamics in Aging Soft Matter. *Faraday Discuss.* 2003,
 123 (1), 237–251.

- (31) Cipelletti, L.; Manley, S.; Ball, R. C.; Weitz, D. A. Universal Aging Features in the Restructuring of Fractal Colloidal Gels. *Phys. Rev. Lett.* **2000**, *84* (10), 2275–2278.
- (32) Falus, P.; Borthwick, M. A.; Narayanan, S.; Sandy, A. R.; Mochrie, S. G. J. Crossover from Stretched to Compressed Exponential Relaxations in a Polymer-Based Sponge Phase. *Phys. Rev. Lett.* **2006**, *97* (6), 1–4.
- (33) KGaA., H. A. & C. Dual Cure Epoxy Formulations for 3D Printing Applications. PCT/EP2020/063127, 2020.
- (34) Invernizzi, M.; Natale, G.; Levi, M.; Turri, S.; Griffini, G. UV-Assisted 3D Printing of Glass and Carbon Fiber-Reinforced Dual-Cure Polymer Composites. *Materials (Basel)*. **2016**, *9* (7), 583
- (35) Chen, K.; Kuang, X.; Li, V.; Kang, G.; Qi, H. J. Fabrication of Tough Epoxy with Shape Memory Effects by UV-Assisted Direct-Ink Write Printing. *Soft Matter* **2018**, *14* (10), 1879–1886.
- (36) Chen, K.; Zhang, L.; Kuang, X.; Li, V.; Lei, M.; Kang, G.; Wang, Z. L.; Qi, H. J. Dynamic Photomask-Assisted Direct Ink Writing Multimaterial for Multilevel Triboelectric Nanogenerator. *Adv. Funct. Mater.* **2019**, *29* (33), 1–9.
- (37) Park, C. H.; Lee, S. W.; Park, J. W.; Kim, H. J. Preparation and Characterization of Dual Curable Adhesives Containing Epoxy and Acrylate Functionalities. *React. Funct. Polym.* **2013**, *73* (4), 641–646.
- (38) Abeykoon, S. K.; Zhang, Y.; Dill, E. D.; Caswell, T. A.; Allan, D. B.; Akilic, A.; Wiegart, L.; Wilkins, S.; Heroux, A.; Van Dam, K. K.; Sutton, M.; Fluerasu, A. Software Tools for X-Ray Photon Correlation and X-Ray Speckle Visibility Spectroscopy. 2016 New York Sci. Data Summit, NYSDS 2016 Proc. 2016.

- (39) Madsen, A.; Leheny, R. L.; Guo, H.; Sprung, M.; Czakkel, O. Beyond Simple Exponential Correlation Functions and Equilibrium Dynamics in X-Ray Photon Correlation Spectroscopy. *New J. Phys.* **2010**, *12*. 055001
- (40) Malik, A.; Sandy, A. R.; Lurio, L. B.; Stephenson, G. B.; Mochrie, S. G. J.; Mc Nulty, I.; Sutton, M. Coherent X-Ray Study of Fluctuations during Domain Coarsening. *Phys. Rev. Lett.* **1998**, *81* (26), 5832–5835.
- (41) Ehrburger-Dolle, F.; Morfin, I.; Bley, F.; Livet, F.; Heinrich, G.; Richter, S.; Piché, L.; Sutton, M. XPCS Investigation of the Dynamics of Filler Particles in Stretched Filled Elastomers. *Macromolecules* **2012**, *45* (21), 8691–8701.
- (42) Narayanan, R. A.; Thiyagarajan, P.; Lewis, S.; Bansal, A.; Schadler, L. S.; Lurio, L. B. Dynamics and Internal Stress at the Nanoscale Related to Unique Thermomechanical Behavior in Polymer Nanocomposites. *Phys. Rev. Lett.* **2006**, *97* (7), 3–6.
- (43) Hernández, R.; Criado, M.; Nogales, A.; Sprung, M.; Mijangos, C.; Ezquerra, T. A. Deswelling of Poly(N-Isopropylacrylamide) Derived Hydrogels and Their Nanocomposites with Iron Oxide Nanoparticles as Revealed by X-Ray Photon Correlation Spectroscopy. *Macromolecules* **2015**, *48* (2), 393–399.
- (44) Hernández, R.; Nogales, A.; Sprung, M.; Mijangos, C.; Ezquerra, T. A. Slow Dynamics of Nanocomposite Polymer Aerogels as Revealed by X-Ray Photocorrelation Spectroscopy (XPCS). J. Chem. Phys. 2014, 140 (2). 024909
- (45) Garrahan, J. P.; Chandler, D. Coarse-Grained Microscopic Model of Glass Formers. *Proc. Natl. Acad. Sci. U. S. A.* **2003**, *100* (17), 9710–9714.